Research Article | Vol. 32, No. 21 / 7 Oct 2024 / Optics Express 37001
Optics EXPRESS

20 µm resolution multipixel ghost imaging with high-energy x-rays

O. Sefi,[1,4] A. Ben Yehuda,[1] Y. Klein,[1,2] Z. Sobol,[1] S. Bloch,[3] H. Schwartz,[1] E. Cohen,[3] and S. Shwartz[1,5]

[1]Physics Department and Institute of Nanotechnology and Advanced Materials, Bar-Ilan University, Ramat Gan 52900, Israel
[2]Nexus for Quantum Technologies, University of Ottawa, Ottawa, Ontario K1N 6N5, Canada
[3]Faculty of Engineering and Institute of Nanotechnology and Advanced Materials, Bar-Ilan University, Ramat Gan 52900, Israel
[4]sefior@biu.ac.il
[5]sharon.shwartz@biu.ac.il

Abstract: Hard x-ray imaging is indispensable across diverse fields owing to its high penetrability. However, the resolution of traditional x-ray imaging modalities, such as computed tomography (CT) systems, is constrained by factors including beam properties, the limitations of optical components, and detection resolution. As a result, the typical resolution in commercial imaging systems that provide full-field imaging is limited to a few hundred microns, and scanning CT systems are too slow for many applications. This study advances high-photon-energy imaging by extending the concept of computational ghost imaging to multipixel ghost imaging with x-rays. We demonstrate a remarkable resolution of approximately 20 µm for an image spanning 0.9 by 1 cm^2, comprised of 400,000 pixels and involving only 1000 realizations. Furthermore, we present a high-resolution CT reconstruction using our method, revealing enhanced visibility and resolution. Our achievement is facilitated by an innovative x-ray lithography technique and the computed tiling of images captured by each detector pixel. Importantly, this method maintains reasonable timeframes and can be scaled up for larger images without sacrificing the short measurement time, thereby opening intriguing possibilities for noninvasive high-resolution imaging of small features that are invisible with the present modalities.

1. Introduction

Hard x-rays offer unparalleled vision through opaque materials, enabling examination of elements invisible to longer wavelengths due to strong absorption. However, this advantage faces a hurdle in full-field imaging of large objects. The main challenge lies in the inherently small numerical aperture and reflectivity of optical components, which render them ineffective for the imaging of large objects [1]. Focusing and scanning with x-rays is possible through various techniques [1], but the scanning process is time-intensive due to the inherent tradeoff between resolution and field of view, hence scanning is impractical for large objects.

To circumvent these limitations, x-ray imaging systems employ cone beams that diverge and cover the large object. The resolution is mostly constrained by the resolution of the camera and by the size of the source [2]. On the detector side, the resolution is constrained by both the pixel size and by the thickness of the scintillation screen, responsible for converting x-rays into visible radiation. Regrettably, especially at high photon energies, thick scintillators are necessary to uphold a sufficiently high detection efficiency [3]. As a result, scattering within the scintillator introduces blurring in the detected image. The standard resolution in current x-ray imaging full-field modalities is typically around a few hundred microns [2]. While this is suitable for various types of measurements, it hinders the ability to detect smaller features, such as microscopic cracks in materials or sub-millimeter subtle anomalies in organs. It is worth

#524414 https://doi.org/10.1364/OE.524414
Journal © 2024 Received 27 Mar 2024; accepted 19 Aug 2024; published 30 Sep 2024

Optics EXPRESS

noting that while high-resolution imaging systems, such as micro-CT systems, do exist, they either feature a small field of view or necessitate lengthy measurement times [4,5]. Current research endeavors aimed at resolution enhancement focus on the development of highly efficient scintillators, which can be made thinner, thus minimizing scattering effects [3]. Exploring alternative pathways for resolution enhancement, such as refining x-ray sources and incorporating better optical elements is an active field of research [6].

An alternative approach to achieve this goal involves the utilization of coded apertures or patterned illumination, employing nonuniformity to the beam to enhance image properties [7,8]. Ghost imaging (GI) is one such imaging modality, which utilizes intensity variations in the beam to retrieve the spatial information of an object. In classical GI a pair of identical nonuniform beams is used. One beam, known as the reference, is directed straight to a camera. The other beam, referred to as the test, illuminates an object and is captured by a single-pixel detector. This process is repeated multiple times with different light patterns. The image is then reconstructed by correlating the detected signals with the transmitted light patterns [9]. In its early days, GI was demonstrated with quantum light [10]. It was later extended to other types of radiation, such as thermal light, x-rays, atoms, neutrons, electrons, fluorescence, and scattered radiation [9,11–16]. Additionally, GI was extended to other domains, such as spectroscopy, diffraction imaging, polarization and temporal measurements, tomography, and object classification [16–25]. In one important variation of GI, called computational ghost imaging (CGI), the light patterns are introduced to the beam using a known mask, removing the need for their detection [26–28]. As the intensity patterns are known a single-pixel detector is sufficient for the image reconstruction.

One of the main challenges in GI lies in the number of intensity patterns needed, since it is proportional to the total number of pixels in the image. Despite the improved performance of current reconstruction algorithms in terms of compression ratio (the ratio between the number of reconstructed pixels to the number of measurements) [29–34], a substantial number of light patterns is still necessary. The current approach leads to an extended measurement process, rendering previous methods for applying x-ray GI impractical for most applications. Significantly reducing the measurement time is a crucial step for advancing further developments in x-ray GI.

The second crucial challenge revolves around the modulation depth of light patterns. While in GI at optical wavelengths, achieving high-contrast intensity modulation is easily accomplished using Spatial Light Modulators, the absence of these components in the x-ray region poses a significant obstacle. In x-ray GI modulation is commonly achieved by directing x-rays through materials with a porous or grainy structure, or by using specially fabricated masks. To attain high resolution and contrast simultaneously, the features in the mask must be tall and narrow, with the height determining the modulation depth and the width affecting the feature size of the intensity patterns and thus the resolution. However, the inherent instability and the small dimensions of these structures making them difficult to produce by standard techniques [35]. All prior efforts in x-ray GI have concentrated on photon energies below 30 keV [11,28,36,37]. However, this limitation proves to be impractical for many non-invasive x-ray measurements and medical imaging, for which a large penetration depth is required.

In this work, we present a proof-of-principle experiment demonstrating a method to overcome the two critical challenges described above and showcase its applicability for standard x-ray sources and flat panel detectors (FPDs). Our method leverages the multi-pixel CGI approach, similarly to the ideas presented in the optical region and with neutrons [11,36,37], achieving high resolution. The high-resolution modulation of the x-ray beam is enabled by a custom-designed mask fabricated through advanced x-ray lithography [38]. This mask, featuring incredibly tall and narrow features known as high aspect ratio structures, plays a crucial role in achieving the desired resolution. Unlike conventional GI, with our approach the number of measurements scales with the enhancement in resolution instead of the total number of pixels. This method, therefore,

Optics EXPRESS

enables high-resolution reconstruction of image with a large field of view in a reasonable time frame.

2. Experimental setup and image reconstruction

The experimental setup consists of a commercial tungsten x-ray tube (IXS1650 from VJ X-Ray Ltd.) set to a current of 2 mA, that emits a cone beam with a peak photon energy of 80 keV, a shutter, a custom-designed gold mask, and an FPD (NDT0909 M from iRay Technology Co. Ltd.) featuring a pixel pitch of 205 μm and a measured resolution of approximately 500 μm, as shown in Fig. 1(a). Additionally, we used a Zaber a X-RSW60A rotation stage to align the sample with respect to FPD, with accuracy of 0.07 degrees. The mask we used consists of rectangular 100 ± 10 μm tall gold pillars with a width of 15 ± 1.5 μm on a silicon substrate that is 525 μm thick. This height results in a modulation depth of approximately 50%, which is sufficient for our purpose. The mask spanned a total area of 1.4 ×1.5 cm^2. We designed the mask in segments, each containing a random matrix, while ensuring that different parts of the mask contain new information. The mask was fabricated by Microworks GmbH using state-of-the-art x-ray lithography. This technique allows for the fabrication of 3D structures with high accuracy and large aspect ratios, thanks to the deep penetration capabilities of the x-rays [38]. A high-resolution image of a segment from the mask is show in Fig. 1(b). The mask was positioned on two Thorlabs LTS150 translation stages (one horizontal and one vertical), with a precision of ±5 μm. The x-ray source was positioned approximately 1 m away from the mask, which was positioned approximately 2 cm from the object, so that penumbra effects are neglectable. The distance between the mask and the FPD was about 2 cm. We reconstructed the image by capturing low-resolution images of the object with the FPD for various positions of the mask, each corresponding to a different pre-designed illumination pattern [39].

For each of the segments we defined, the image reconstruction was accomplished by solving the linear inverse problem, while using compressive sensing (CS) and the total variation (TV) as a constraint [29,30,40]. The TV problem can be formulated as the minimization task of:

$$TV = \mu\|Ax - B\|_2 + \lambda_1\|\nabla_x x\|_1 + \lambda_2\|\nabla_y x\|_1 \quad (1)$$

Here, the illumination patterns are represented by the matrix A, in which every row is a single light pattern, the vector x represents the unknown transmission function of the object, and B is a vector representing the detected test signals. The terms $\|\ldots\|_2$ and $\|\ldots\|_1$ are the L2 and L1 norms, respectively, and ∇_x and ∇_y represent the first derivatives in the x and y directions. The parameters μ and λ serve as regularization factors, which balance between the actual measurements and the smoothing constraints captured by the spatial derivatives. Here, the resolution of the reconstructed x is determined by the feature size of the mask [18].

A schematic description of the reconstruction workflow is shown in Fig. 1(c). First, we applied the TV reconstruction algorithm to each set of few adjacent pixels on the FPD, which results in a series of partially overlapping local images. Finally, we assembled all the tiles, using nonlinear blending, to create a complete high-resolution image with a large field of view [41]. Further details on the reconstruction procedures are presented in Supplement 1.

Optics EXPRESS

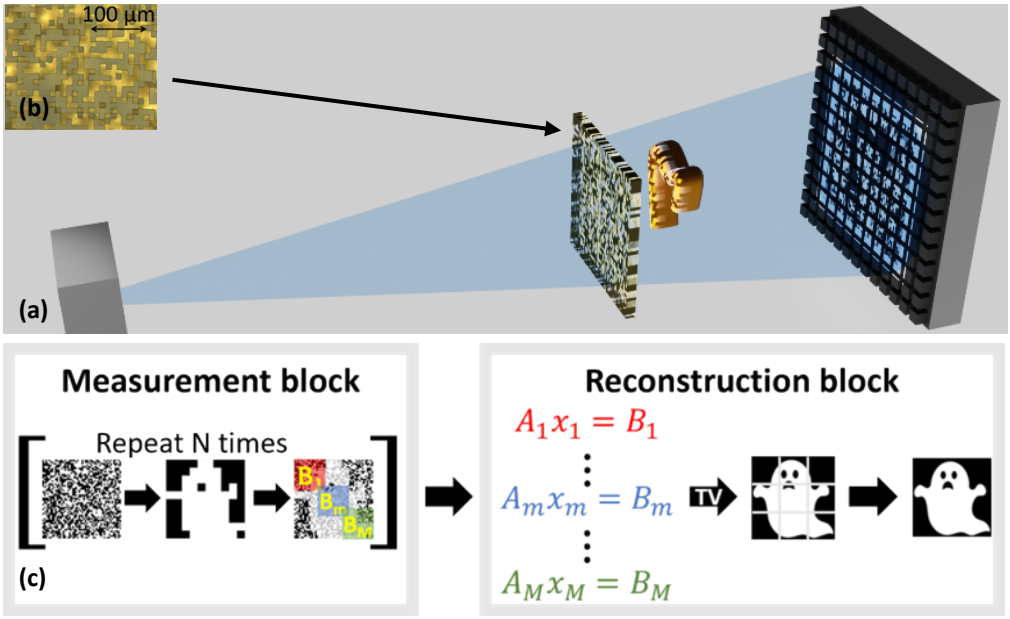

Fig. 1. (a) Schematic description of the experimental system. The cone beam propagates from left to right, impinges upon a mask that introduces inhomogeneous patterns on the object. The radiation transmitted through the object is collected by an FPD. (b) A magnified image of a segment from our mask. (c) Schematic description of the measurement and analysis process. N different light patterns illuminate the object and are collected by the FPD with each set of a few adjacent pixels serving as a bucket detector. The TV algorithm is used to solve the GI equations within each bucket area, resulting in a series of partially overlapping local images. Finally, the overlap is used to smoothly assemble all the tiles, forming the complete high-resolution image.

3. Results

To demonstrate the advantages of our approach in reconstructing large images at enhanced resolution, we imaged a copper wire with a minimum thickness of ~130 µm and total area of about 1×1 cm^2. We binned each 5×5 pixel block of the FPD to form an array of partially overlapping bucket detectors. The chosen block size is optimal for our system, striking a balance that ensures a reasonably low compression ratio while minimizing undesirable effects arising from the boundaries. These effects may result from sub-FPD-pixel misalignment of the mask or the nonuniform response of the FPD within the pixel size. The low-resolution FPD image and the high-resolution reconstruction are shown in Fig. 2(a) and (b), respectively. The superior resolution of our method is evident. Previously obscured features like thin edges of the copper wire are now clearly resolved and exhibit high contrast in the reconstructed image, as further supported by the cross-sections of Fig. 2(c) and (d). In these cross-sections the green and the red dots represent the data from the FPD, and the purple and blue dots represent the data from our reconstruction. More importantly, the limitations of the FPD image with its low resolution are overcome by our method, which unveils intricate details significantly smaller than the FPD pixel size.

Furthermore, even though the resulting image in Fig. 2(b) comprises approximately 400,000 pixels, it was reconstructed using only 1000 realizations with exposure time of 4 seconds per realization. Given that the measurement time is independent of the number of segments, this

Optics EXPRESS

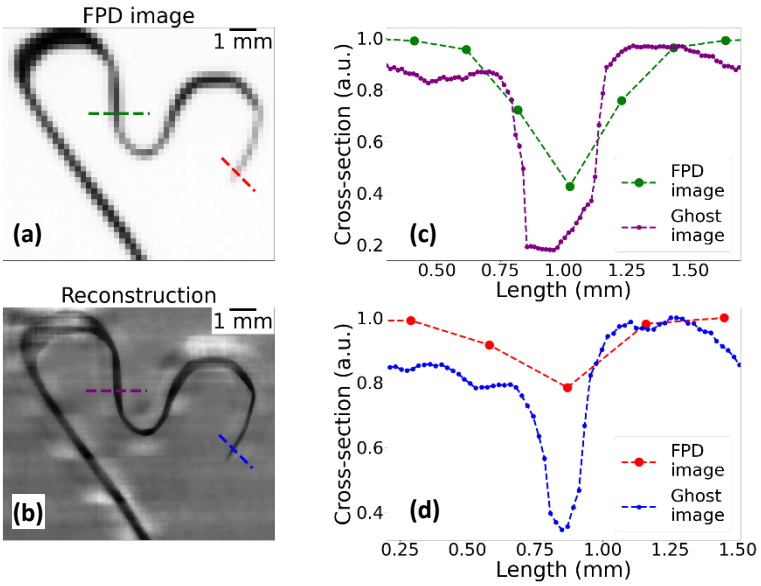

Fig. 2. (a) The image of a copper wire captured with the FPD. (b) The high-resolution reconstruction with the multipixel GI approach. (c) and (d) Cross-sections along the dashed lines with the corresponding colors in the images. In these cross-sections, the green and the red dots represent the FPD, and the purple and the blue dots represent the reconstruction. The dashed lines serve as guides to the eye.

implies that our method is capable of reconstructing images with a pixel count commonly found in noninvasive imaging, all within acceptable measurement times.

To quantitatively assess the resolution of our reconstruction, we examined the blurring of a sharp edge of a 0.7 mm thick polished silicon wafer, positioned on the rotation stage. The uncertainty of the angle of the rotation stage corresponds to blurring of about 15 µm on the FPD. The FPD image of the silicon wafer and a high-resolution reconstruction are shown in Fig. 3(a) and (b). The cross-sections are depicted in Fig. 3(c), where the green and red dots correspond to measurements by the FPD, and our reconstruction, respectively. By measuring the half-width of the slope of the cross-section near the edge, we estimate the resolution to be approximately 20 µm. This result is consistent with the feature size of the mask.

We acknowledge that, in principle, the number of realizations can be further reduced based on the specific object and the prior knowledge about it, and improvements can be achieved through advanced reconstruction algorithms. To assess the impact of the number of realizations on the quality of the reconstructed image, we deliberately chose smaller subsets from our realizations. We conducted multiple reconstructions of a segment from the copper wire, each time utilizing different realizations while maintaining the subset size. The goal of this process is to obtain multiple reconstructions under similar imaging conditions, from which we can derive statistical data on the reconstruction quality. We compute the mean squared error (MSE) and its standard deviation in relation to the optimal reconstruction generated from 1000 realizations. We continue this process with subsets of increasing size to demonstrate the dependency of the reconstruction on the number of realizations. The results are shown in Fig. 3(d). Here, the blue dots represent the MSE from the best image and the vertical error-bars represent its standard deviations. In the insets the reconstructions with 20, 150, 500 and 1000 realizations are shown form left to right, respectively. It is evident that the significant improvement in the image occurs after about 500 realizations, which corresponds to a compression ratio of about 10 within each 5×5 pixel

Optics EXPRESS

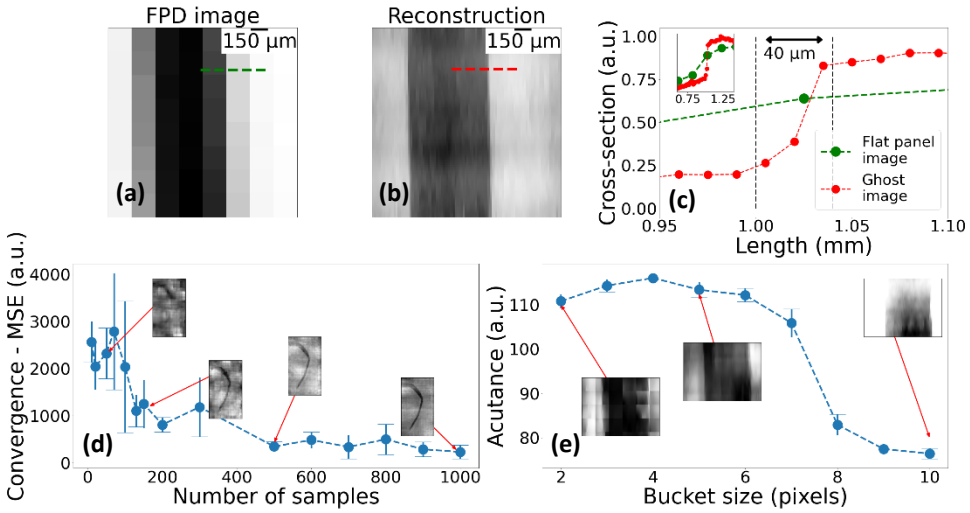

Fig. 3. (a) FPD image of the silicon wafer. (b) High-resolution reconstruction with the multipixel GI approach. (c) Cross-section along the dashed lines. The green dots represent the FPD, and the red dots represent the reconstruction. In the inset, the zoomed-out cross-section is shown. (d) MSE of the copper wire images dependence on the number of realizations. The blue dots represent the MSE, and the vertical error-bars represent its standard deviation. Insets (left to right): reconstructions with 20, 150, 500, and 1000 realizations. (e) Acutance of the reconstructed silicon wafer image vs. bucket size. Blue dots represent the acutance and vertical error-bars represent its standard deviation. Insets (left to right): Reconstructions with bucket sizes of 2, 5 and 10 FPD pixels. Dashed lines serve as guides to the eye.

block of the FPD. This result can be further improved by using better reconstruction algorithms [42–44].

The results presented above were obtained using a bucket size of 5×5 pixels. However, since we use a multi-pixel detector for the multi-pixel GI, a question raises: is there an optimal bucket size that optimizes the quality of the images for a chosen number of realizations? This is because we aim to reduce the number of realizations to reduce the measurement time, but in GI the quality of image improves with the number of realizations. This consideration suggests that the best choice would be one pixel of the FPD. However, due to scattering from the scintillation screen of the FPD the point spread function of the detector is larger than one pixel, which suggests that selecting one pixel is not the optimal choice. In addition, our reconstruction algorithms also strongly depend on the size of the pixel due to the degree of sparsity and overlap issues and small bucket sizes are more susceptible to errors in the sub-FPD-pixel-size positioning of the mask. To address this question, we show the dependence of the reconstructed image on the bucket size in Fig. 3(e). We calculated the acutance of the reconstructed silicon edge, which is the mean value of the image gradient, approximated by the Sobel filter [45–47]. We repeated this for different bucket sizes ranging from 2×2 to 10×10 FPD pixels. We reiterated the validation process mentioned above for each bucket size by using 1000 different realizations. In Fig. 3(e), the blue dots correspond to the acutance, and the vertical error-bars represent its standard deviations. The insets show the reconstructed images for buckets sizes of 2×2, 5×5 and 10×10 FPD pixels, from left to right, respectively. We concluded that for our system, the optimum is for buckets of 5×5 FPD pixels, a number that may vary for different systems and different reconstruction algorithms.

Optics EXPRESS

To further demonstrate the power of our method, we performed a high-resolution computational tomography (CT) reconstruction of an M4 screw with a washer and half a nut. The 3D reconstructed volume has dimensions of about $8.6 \times 8.6 \times 8.8$ mm^3 (L×W×H) and contains approximately $2 \cdot 10^8$ voxels. We used 73 projections, each with 1089 realizations, for the reconstruction. We reconstructed each projection separately, and the CT reconstruction was performed using the TIGRE toolbox [48]. Figure 4 presents the tomograms, with the top row showing reconstructions from the FPD images and the bottom row displaying those from our high-resolution images. Specifically, panels (a) and (b) depict a top-view slice of the bisected nut, panels (c) and (d) illustrate a front-view slice, and panels (e) and (f) reveal a side-view slice. More tomograms are shown in Fig. S1 in Supplement 1 and in Visualization 1, Visualization 2 and Visualization 3. Clearly, our method significantly enhances the visibility of fine details, such as the hexagonal shape of the nut and the pitch of the screw, which are barely discernible in the FPD CT reconstruction.

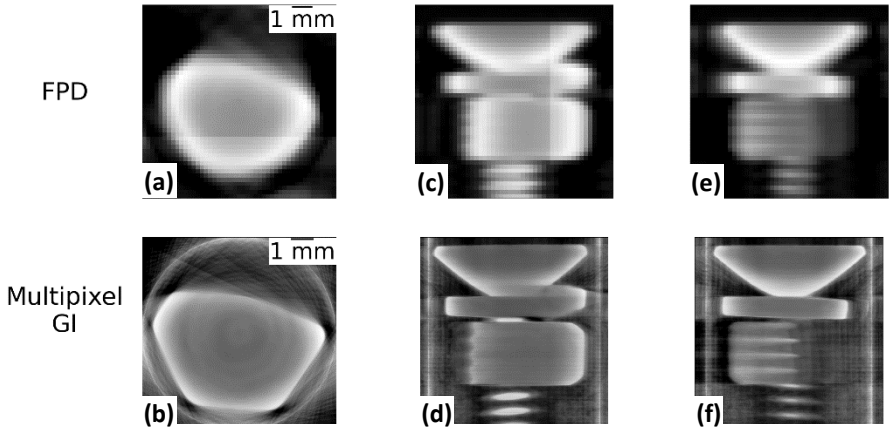

Fig. 4. Comparison between tomograms of an M4 screw reconstructed using the FPD (top row) and using our multipixel GI method (bottom row). The tomograms are shown from top view (a) and (b), from front view (c) and (d) and from side view (e) and (f).

Our technique exhibits a notable enhancement in resolution when compared to conventional high-photon-energy full-field x-ray tube-based modalities. While one could argue that similar resolution might be achievable, in principle, with other techniques like raster scan or single-pixel GI, the practical considerations and additional advantages of our approach set it apart. Due to the inherent dose reduction capabilities of the CS approach, and by optimizing the diffuser, high-quality images can be achieved in shorter measurement times compared to current state-of-the-art systems [49,50]. Additionally, increasing the field of view in our scheme can be done simply by increasing the size of the mask, with no implications on the acquisition time or the resolution.

To highlight the practical merits of our approach, we compare the estimated exposure time of our method with those of single-pixel GI and one projection from a micro-CT scan in Table 1. We used simulations of an image containing 10^6 pixels with a resolution of 20 µm. The comparison is done while maintaining a similar compression ratio for single-pixel GI. In this comparison we used typical exposure time for a micro-CT image and assumed a typical cone beam with flux of 10^{10} photons/second [51,52].

The conclusion drawn from Table 1 is clear and decisive. Our approach demonstrates significantly shorter measurement times and requires much less dose compared to single-pixel GI and maintains comparable timescales to micro-CT scans. However, we emphasize that unlike standard scanning micro-CT, our approach does not have increased exposure time for a larger field of view. Therefore, our method is expected to significantly outperform micro-CT for large

Optics EXPRESS

Table 1. Comparison between multi-pixel GI and single-pixel GI and micro-CT[a].

	Number of sampling points	Exposure time for 1 projection (sec)
Micro-CT	$\sim 10^6$	~0.5
Single-pixel GI	5×10^4	~200
Multi -pixel GI	170	~0.5

[a]Estimated total exposure times for a micro-CT projection, single-pixel GI, and multi-pixel. Details are shown in Supplement 1.

objects. The primary challenges associated with single-pixel GI, such as measurement time and Contrast-to-Noise Ratios due to the requirement for a large number of features in the mask [39], are effectively addressed by our approach. This marks a significant advancement toward the practical application of structured illumination approaches at high photon energies. Importantly, our method not only demonstrates remarkable speed but also exhibits scalability for larger images with a comparable number of realizations. This scalability can be achieved through mask size expansion using contemporary technologies, further underscoring the potential and versatility of our approach.

Before we conclude, we comment on the impact of the bucket size on the measurement. In GI, there is a fundamental tradeoff between the resolution and the SNR, while the SNR can be improved by increasing the number of measurements [53]. As a direct consequence, higher resolution requires larger number of measurements, i.e., there is a fundamental tradeoff between the resolution enhancement and the number of measurements required to maintain a constant SNR. This can be understood by recalling that GI can be described as a projection of a vector (the object) on a basis. From this description it directly stems that a vector with larger number of elements (i.e., more pixels) requires a larger number of basis vectors, hence more intensity patterns. In large bucket detectors, this constraint results in extended measurement times to maintain the SNR in the image. This consideration highlights the advantage of multiplexing GI. By reducing the number of pixels per bucket, a comparable SNR can be maintained with fewer measurements. However, this consideration also implies that there is a limit to the resolution enhancement. Achieving significant resolution improvements will require more acquisitions, leading to longer measurement times and making the imaging process impractical.

In conclusion, we have introduced and demonstrated a proof-of-concept experiment for an x-ray imaging technique operating at high photon energies, utilizing patterned radiation and intensity correlations. Our method successfully reconstructed high-resolution 2-dimensional images and a 3-dimensional volume, with the former comprising 400,000 pixels reconstructed with 1000 realizations and at exposure times that can be comparable to commercial CT systems. This achievement translates to a remarkable 100-fold reduction in measurement time compared to common CGI, maintaining equivalent object size and resolution. This achievement sums up to a reduction of about $7 \cdot 10^4$ in measurement time for the high-resolution CT compared to single-pixel CGI. Further enhancements in efficiency can be pursued through the integration of additional prior knowledge into reconstruction algorithms or by incorporating advanced deep learning techniques.

Future advancements may focus on achieving even higher resolutions by employing masks with smaller feature sizes, focusing the light patterns, and accounting for effects like beam hardening [54]. Our straightforward setup, showcasing robustness and high-quality image reconstruction, unlocks unprecedented capabilities for high resolution imaging and CT, at high photon energies. This enables the visualization of minute features currently beyond the reach of existing methods. Examples for applications that would particularly benefit from our modality include high-resolution non-destructive imaging and mammography.

Funding. Israel Innovation Authority; Israel Science Foundation (847/21); PAZY Foundation (5100049579).

Optics EXPRESS

Disclosures. The authors declare no conflicts of interest.

Data availability. Data underlying the results presented in this paper are not publicly available at this time but may be obtained from the authors upon reasonable request.

Supplemental document. See Supplement 1 for supporting content.

References

1. A. Guilherme, G. Buzanich, and M. L. Carvalho, "Focusing systems for the generation of X-ray micro beam: An overview," Spectrochim Acta Part B At Spectrosc. **77**, 1–8 (2012).
2. W. Huda and R. B. Abrahams, "X-Ray-Based Medical Imaging and Resolution," Am. J. Roentgenol. **204**(4), W393–W397 (2015).
3. L. Wollesen, F. Riva, P.-A. Douissard, *et al.*, "Scintillating thin film design for ultimate high resolution X-ray imaging," J. Mater Chem C Mater **10**(24), 9257–9265 (2022).
4. K. Keklikoglou, C. Arvanitidis, G. Chatzigeorgiou, *et al.*, "Micro-CT for Biological and Biomedical Studies: A Comparison of Imaging Techniques," J. Imaging **7**(9), 172 (2021).
5. D. P. Clark and C. T. Badea, "Advances in micro-CT imaging of small animals," Physica Medica. **88**, 175–192 (2021).
6. A. Sakdinawat and D. Attwood, "Nanoscale X-ray imaging," Nat. Photonics **4**(12), 840–848 (2010).
7. E. Mojica, C. V. Correa, and H. Arguello, "High-resolution coded aperture optimization for super-resolved compressive x-ray cone-beam computed tomography," Appl. Opt. **60**(4), 959 (2021).
8. J. Li, S. Chen, D. Ratner, *et al.*, "Nanoscale chemical imaging with structured X-ray illumination," Proc. Natl. Acad. Sci. **120**(49), e2314542120 (2023).
9. A. Valencia, G. Scarcelli, M. D'Angelo, *et al.*, "Two-Photon Imaging with Thermal Light," Phys. Rev. Lett. **94**(6), 063601 (2005).
10. T. B. Pittman, Y. H. Shih, D. V. Strekalov, *et al.*, "Optical imaging by means of two-photon quantum entanglement," Phys. Rev. A **52**(5), R3429–R3432 (1995).
11. D. Pelliccia, A. Rack, M. Scheel, *et al.*, "Experimental X-Ray Ghost Imaging," Phys. Rev. Lett. **117**(11), 113902 (2016).
12. R. I. Khakimov, B. M. Henson, D. K. Shin, *et al.*, "Ghost imaging with atoms," Nature **540**(7631), 100–103 (2016).
13. A. M. Kingston, G. R. Myers, D. Pelliccia, *et al.*, "Neutron ghost imaging," Phys. Rev. A **101**(5), 053844 (2020).
14. S. Li, F. Cropp, K. Kabra, *et al.*, "Electron Ghost Imaging," Phys. Rev. Lett. **121**(11), 114801 (2018).
15. Y. Klein, O. Sefi, H. Schwartz, *et al.*, "Chemical element mapping by x-ray computational ghost fluorescence," Optica **9**(1), 63 (2022).
16. A. Ben-Yehuda, O. Sefi, Y. Klein, *et al.*, "High-resolution computed tomography with scattered X-ray radiation and a single pixel detector," Commun. Eng. **3**(1), 39 (2024).
17. Y. Klein, E. Strizhevsky, F. Capotondi, *et al.*, "High-resolution absorption measurements with free-electron lasers using ghost spectroscopy," in *Frontiers in Optics + Laser Science 2022 (FIO, LS)* (Optica Publishing Group, 2022), p. LW7F.4.
18. F. Ferri, D. Magatti, A. Gatti, *et al.*, "High-Resolution Ghost Image and Ghost Diffraction Experiments with Thermal Light," Phys. Rev. Lett. **94**(18), 183602 (2005).
19. P. Janassek, S. Blumenstein, and W. Elsäßer, "Recovering a hidden polarization by ghost polarimetry," Opt. Lett. **43**(4), 883 (2018).
20. P. Ryczkowski, M. Barbier, A. T. Friberg, *et al.*, "Ghost imaging in the time domain," Nat. Photonics **10**(3), 167–170 (2016).
21. O. Sefi, Y. Klein, E. Strizhevsky, *et al.*, "X-ray imaging of fast dynamics with single-pixel detector," Opt. Express **28**(17), 24568 (2020).
22. A. M. Kingston, D. Pelliccia, A. Rack, *et al.*, "Ghost tomography," Optica **5**(12), 1516 (2018).
23. C. Abbattista, L. Amoruso, S. Burri, *et al.*, "Towards Quantum 3D Imaging Devices," Appl. Sci. **11**(14), 6414 (2021).
24. G. Massaro, P. Mos, S. Vasiukov, *et al.*, "Correlated-photon imaging at 10 volumetric images per second," Sci. Rep. **13**(1), 12813 (2023).
25. J.-N. Cao, Y.-H. Zuo, H.-H. Wang, *et al.*, "Single-pixel neural network object classification of sub-Nyquist ghost imaging," Appl. Opt. **60**(29), 9180 (2021).
26. J. H. Shapiro, "Computational ghost imaging," Phys. Rev. A **78**(6), 061802 (2008).
27. Y. Bromberg, O. Katz, and Y. Silberberg, "Ghost imaging with a single detector," Phys. Rev. A **79**(5), 053840 (2009).
28. Y. Klein, A. Schori, I. P. Dolbnya, *et al.*, "X-ray computational ghost imaging with single-pixel detector," Opt. Express **27**(3), 3284 (2019).
29. Y. Sher, "Review of Algorithms for Compressive Sensing of Images," arXiv, (2019).
30. O. Katz, Y. Bromberg, and Y. Silberberg, "Compressive ghost imaging," Appl. Phys. Lett. **95**(13), 131110 (2009).
31. V. Katkovnik and J. Astola, "Compressive sensing computational ghost imaging," J. Opt. Soc. Am. A **29**(8), 1556 (2012).
32. I. Petrelli, F. Santoro, G. Massaro, *et al.*, "Compressive sensing-based correlation plenoptic imaging," Front. Phys. **11**, 1 (2023).

Optics EXPRESS

33. L. Jiying, Z. Jubo, L. Chuan, *et al.*, "High-quality quantum-imaging algorithm and experiment based on compressive sensing," Opt. Lett. **35**(8), 1206 (2010).
34. F. Scattarella, D. Diacono, A. Monaco, *et al.*, "Deep learning approach for denoising low-SNR correlation plenoptic images," Sci. Rep. **13**(1), 19645 (2023).
35. T. Mappes, S. Achenbach, and J. Mohr, "X-ray lithography for devices with high aspect ratio polymer submicron structures," Microelectron. Eng. **84**(5-8), 1235–1239 (2007).
36. A. Schori and S. Shwartz, "X-ray ghost imaging with a laboratory source," Opt. Express **25**(13), 14822 (2017).
37. M. P. Olbinado, D. M. Paganin, Y. Cheng, *et al.*, "X-ray phase-contrast ghost imaging using a single-pixel camera," Optica **8**(12), 1538 (2021).
38. A. Bharti, A. Turchet, and B. Marmiroli, "X-Ray Lithography for Nanofabrication: Is There a Future?" Front. Nanotechnol. **4**, 1 (2022).
39. M.-J. Sun, H.-Y. Wang, and J.-Y. Huang, "Improving the performance of computational ghost imaging by using a quadrant detector and digital micro-scanning," Sci. Rep. **9**(1), 4105 (2019).
40. A. Ribes and F. Schmitt, "Linear inverse problems in imaging," IEEE Signal Process. Mag. **25**(4), 84–99 (2008).
41. S. Preibisch, S. Saalfeld, and P. Tomancak, "Globally optimal stitching of tiled 3D microscopic image acquisitions," Bioinformatics **25**(11), 1463–1465 (2009).
42. S. Liu, X. Meng, Y. Yin, *et al.*, "Computational ghost imaging based on an untrained neural network," Opt. Lasers Eng. **147**, 106744 (2021).
43. H. Wu, G. Zhao, M. Chen, *et al.*, "Hybrid neural network-based adaptive computational ghost imaging," Opt Lasers Eng **140**, 106529 (2021).
44. F. Wang, C. Wang, M. Chen, *et al.*, "Far-field super-resolution ghost imaging with a deep neural network constraint," Light: Sci. Appl. **11**(1), 1 (2022).
45. R. M. Rangayyan, N. M. El-Faramawy, J. E. L. Desautels, *et al.*, "Measures of acutance and shape for classification of breast tumors," IEEE Trans. Med. Imaging **16**(6), 799–810 (1997).
46. R. Ranjan and V. Avasthi, "Edge Detection Using Guided Sobel Image Filtering," Wirel. Pers Commun. **132**(1), 651–677 (2023).
47. R. O. Duda, P. E. Hart, and D. G. Stork, *Pattern Classification* (2000).
48. A. Biguri, M. Dosanjh, S. Hancock, *et al.*, "TIGRE: a MATLAB-GPU toolbox for CBCT image reconstruction," Biomed. Phys. Eng. Express **2**(5), 055010 (2016).
49. A. M. Kingston, W. K. Fullagar, G. R. Myers, *et al.*, "Inherent dose-reduction potential of classical ghost imaging," Phys. Rev. A **103**(3), 033503 (2021).
50. A. M. Kingston, A. Aminzadeh, L. Roberts, *et al.*, "Optimizing nonconfigurable, transversely displaced masks for illumination patterns in classical ghost imaging," Phys. Rev. A **107**(2), 023524 (2023).
51. M. Heyndrickx, T. Bultreys, W. Goethals, *et al.*, "Improving image quality in fast, time-resolved micro-CT by weighted back projection," Sci. Rep. **10**(1), 18029 (2020).
52. S. Prabhu, D. K. Naveen, S. Bangera, *et al.*, "Production of X-RAYS using X-RAY Tube," J. Phys. Conf. Ser. **1712**(1), 012036 (2020).
53. D. Ceddia and D. M. Paganin, "Random-matrix bases, ghost imaging, and x-ray phase contrast computational ghost imaging," Phys. Rev. A **97**(6), 062119 (2018).
54. H. Li, W. Hou, Z. Ye, *et al.*, "Resolution-enhanced x-ray ghost imaging with polycapillary optics," Appl. Phys. Lett. **123**(14), 141101 (2023).